

# Thermal emission from low-field neutron stars

B.T. Gänsicke<sup>1,2</sup>, T.M. Braje<sup>2</sup>, and R.W. Romani<sup>2</sup>

<sup>1</sup> Universitäts-Sternwarte Göttingen, Geismarlandstr. 11, D-37083 Göttingen, Germany

<sup>2</sup> Physics Department, Stanford University, Stanford, CA 94305-4060, USA

Received \_\_\_\_\_; accepted \_\_\_\_\_

**Abstract.** We present a new grid of LTE model atmospheres for weakly magnetic ( $B \lesssim 10^{10}$  G) neutron stars, using opacity and equation of state data from the OPAL project and employing a fully frequency and angle dependent radiation transfer. We discuss the differences to earlier models, including a comparison with a detailed NLTE calculation. As a first application of the new synthetic spectra, we re-analyze the available ROSAT PSPC data of the isolated neutron star candidate RX J1856.5–3754. Our iron and solar abundance model spectra provide satisfactory fits to the X-ray spectrum and are consistent with the distance of RX J1856.5–3754 recently measured by the Hubble Space Telescope, although pulse fractions as small as those observed are difficult to obtain for canonical neutron star radii.

**Key words.** stars: neutron – stars: atmospheres – radiative transfer – radiation mechanisms: thermal

## 1. Introduction

Modern X-ray observatories detect the thermal surface emission of a number of neutron stars. In analogy to the classic model atmosphere analysis of normal stars, such observations permit the direct measurement of fundamental neutron star properties, such as their effective temperatures, atmospheric abundances, and surface gravities. The latter point is especially of great importance, as an accurate measurement of the surface gravity of a neutron star is (with the distance known) equivalent to a measurement of its mass/radius ratio. The observational confirmation/rejection of the predicted neutron star mass-radius relations is a fundamental test of our understanding of the physics of matter above nuclear densities.

The first neutron star model atmospheres involving realistic opacities were computed by Romani (1987, henceforth R87), using atomic data from the Los Alamos Opacity Library and employing a simple angle-averaged radiation transfer. As a major result, R87 could show that the thermal emission of neutron stars differs substantially from a Planck spectrum. For low-metallicity (e.g. helium) atmospheres, the emitted spectrum is harder than the corresponding blackbody spectrum. The spectra emitted from high-metallicity atmospheres (carbon, oxygen or iron) are closer to a blackbody distribution, but show strong absorption structures in the energy range observable with X-ray telescopes.

Rajagopal & Romani (1996, henceforth RR96) computed hydrogen, solar abundance, and iron model atmo-

spheres for low-field neutron stars, using improved opacity and equation of state data from the OPAL project (Iglesias & Rogers 1996), but employing the same radiation transfer as R87. Contemporaneously, a similar set of low-field atmospheres, partially based on the same atomic OPAL data, but employing a more sophisticated radiation transfer, were presented by Zavlin et al. (1996, henceforth ZVS96). The RR96 and ZVS96 models, broadly confirming the results of R87, were applied to X-ray observations of presumably low-field neutron stars, i.e. millisecond pulsars (RR96, Zavlin & Pavlov 1998), isolated neutron stars (Pavlov et al. 1996), and transiently accreting neutron stars in quiescence in LMXBs (e.g., Rutledge et al. 1999, 2000, 2001).

In the case of strongly magnetic neutron stars ( $B \sim 10^{12} - 10^{14}$  G), both the observation and the computation of the thermal surface emission is significantly more difficult, as non-thermal magnetospheric radiation dilutes the surface emission and as little atomic data is readily available (for a review of the properties of matter in strong magnetic fields, see Lai 2001). Magnetic models for hydrogen and iron atmospheres were computed by Pavlov et al. (1995) and Rajagopal et al. (1997), respectively.

The wealth of high-quality neutron star observations expected from *Chandra* and *XMM* necessitates the availability of modern model atmospheres. In this paper, we present new model atmosphere grids for low-field neutron stars that overcome a number of shortcomings and errors in the RR96 and ZVS96 calculations. As a first application of the new models, we re-analyze the ROSAT PSPC spec-

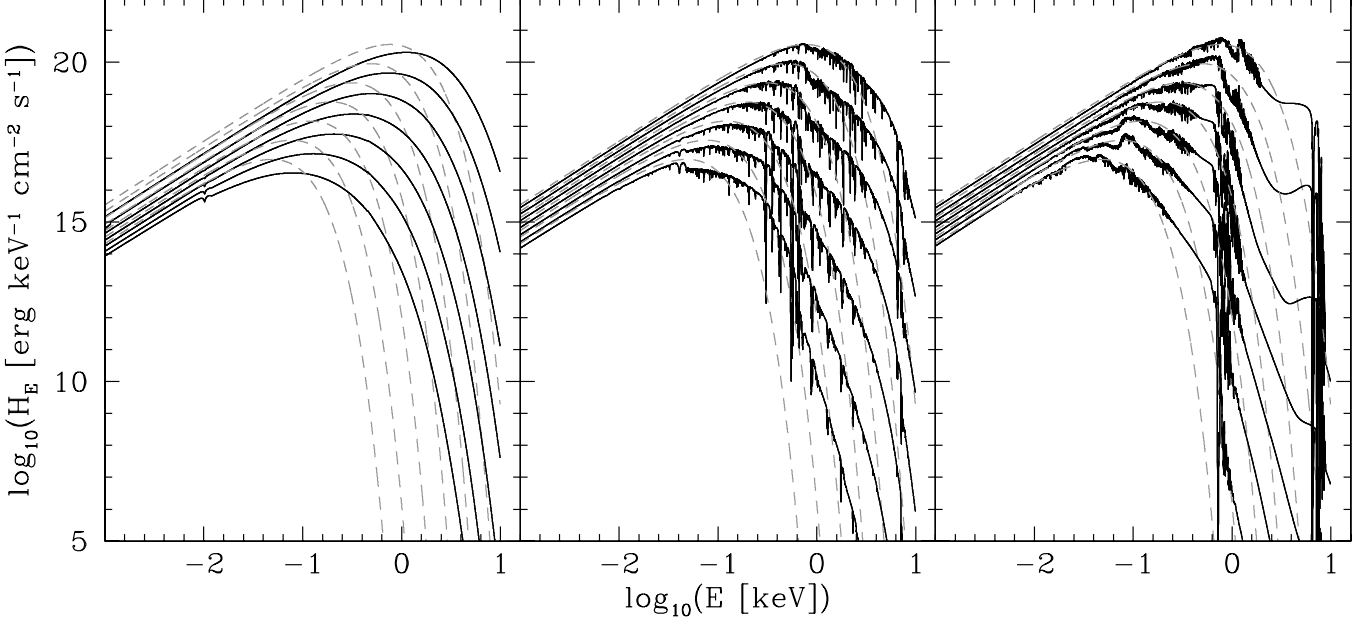


**Fig. 1.** Emergent model spectra (unredshifted Eddington flux) for  $M_{\text{ns}} = 1.4 M_{\odot}$ ,  $R_{\text{ns}} = 10$  km neutron stars. From left to right: hydrogen, solar abundance, and iron atmospheres. From top to bottom in each panel:  $\log T_{\text{ns}} = 6.5, 6.3, 6.1, 5.9, 5.7, 5.5, 5.3$ . Plotted as grey dashed lines are blackbody spectra for the corresponding temperatures.

trum of the isolated neutron star candidate RX J1856.5–3754.

## 2. The model atmospheres

The new grid of neutron star atmospheres was computed combining a fully frequency and angle dependent radiation transfer code and the OPAL opacities from RR96. The employed radiation transfer is part of a model atmosphere code that has previously been used for the computation of white dwarf atmospheres (Gänsicke et al. 1995) which have been widely applied to observations of cataclysmic variables and white dwarf/main-sequence binary stars.

The model atmospheres were created under the following assumptions. (1) Plane-parallel geometry. The atmosphere of a neutron star has a vertical extension of a few centimeters at most, compared to a radius of  $\sim 10$  km. Its curvature is hence completely negligible. (2) Hydrostatic equilibrium. For the extreme surface gravity of neutron stars and the relatively low temperatures that we consider here, the atmosphere is static. The situation is different in accreting neutron stars during X-ray bursts, where the nuclear burning atmosphere considerably expands on short time scales. (3) Radiative equilibrium. The atmosphere contains no source of energy, but acts only as a blanket, through which the thermal energy of the underlying core is leaking out. In Sect. 4, we will discuss how abandoning this assumption will impact the spectrum of the neutron star. (4) Local thermal equilibrium (LTE). For the high densities and the low temperatures in the considered atmospheres collisional ion-ion interactions dominate over interactions between matter and the radiation field throughout most of the atmosphere. Deviations from LTE

in the outermost tenuous layers of the atmosphere may somewhat affect the depth of the absorption lines, but considering the overall level of uncertainty in the involved atomic physics, and the relatively poor quality of the available spectroscopy, the assumption of LTE appears to be a reasonable approximation. Below, we discuss a quantitative comparison to a NLTE model.

With these approximations, the computation of a model atmosphere can be separated into two independent parts: calculating the structure of the atmosphere from the integration of the hydrostatic equation (Sect. 2.1) and solving the radiation transfer (Sect. 2.2). The temperature run through the atmosphere,  $T(z)$ , is a free parameter in the overall process and is adjusted iteratively until radiative and hydrostatic equilibrium are satisfied (Sect. 2.3).

### 2.1. Atmosphere structure

The vertical scale of the atmosphere is transformed from the geometrical depth  $z$  to the optical depth  $\tau$  by  $dz = d\tau/\rho\chi$ , with  $\chi$  the total mean opacity (see below) and  $\rho$  the density. The structure of the atmosphere is then obtained by integrating the equation of hydrostatic equilibrium

$$\frac{dP_g}{d\tau} = \frac{g}{\chi} \quad (1)$$

where  $P_g$  is the gas pressure, from an outer boundary  $\tau_{\min}$  to an inner boundary  $\tau_{\max}$ . Considering the extremely high surface gravity encountered in a neutron star atmosphere, we neglect the effects of radiation pressure. We compute a starting value for the integration of eq. (1),  $P_g(\tau = \tau_{\min})$ , assuming that the outer layers of the at-

mosphere are isothermal and that the degree of ionization is constant. With  $\chi = \text{const.}$

$$P_g(\tau_{\min}) = \frac{g}{\chi(\tau_{\min})} \tau_{\min}. \quad (2)$$

$\chi$  being itself a function of  $(T, P_g)$ , we use  $\chi(\tau_{\min}) = 1$  as an estimate and solve eq. (2) with a Newton-Raphson method. From  $P_g(\tau = \tau_{\min})$  we proceed with the integration of eq. (1) to  $\tau_{\max}$ .

This integration involves at each depth the evaluation of the equation of state (EOS) as well as the computation of the absorption and scattering coefficients. For the EOS and the radiative opacities, we use the OPAL data (Iglesias & Rogers 1996) from RR96, which cover three different chemical compositions: hydrogen, solar abundances, and iron. The opacities are tabulated as a function of the temperature  $T$ ,  $R = \rho/T_6^3$  with  $T_6$  the temperature in  $10^6$  K, and  $u = E_\gamma/k_B T$ , with  $E_\gamma$  the photon energy (for additional details on the OPAL opacity tables, see RR96). For a given depth in the atmosphere, defining  $T$  and  $\rho$ , and a given energy, the radiative absorption coefficient  $\kappa_{\text{rad}}(T, \rho, E)$  is calculated from the opacity tables using a bilinear interpolation in  $\log T$  and  $\log R$  and a linear interpolation in  $E$ . In the construction of the model atmospheres, the radiative absorption coefficient  $\kappa_{\text{rad}}(T, \rho, \delta E)$  for a finite energy interval  $\delta E$  is given by the harmonic mean of  $n$  individual evaluations of  $\kappa_{\text{rad}}(T, \rho, E_n)$ , with  $E_n$  within  $\delta E$ , and  $n$  sufficiently large to sample well the resolution of the OPAL tables. We include Thomson scattering as additional radiative opacity,  $\sigma_e = N_e 6.65 \times 10^{-25} / \rho$ , with  $N_e$  the electron density in  $\text{cm}^{-3}$ . Thomson scattering is an important source of opacity only in low-Z atmospheres at high temperatures and high energies. Finally, we compute a radiative Rosseland mean opacity  $\bar{\kappa}_{\text{Ross}}$  from the OPAL opacity  $\kappa_{\text{rad}}(E)$  and the Thomson scattering  $\sigma_e$ .

Following RR96, we include a conductive opacity  $\kappa_{\text{con}} = (2.5 \times 10^4 / n_e) / (Z^2 / A) (T_7^{1/2} / \rho) \text{cm}^2 \text{g}^{-1}$  (Cox & Giuli 1968) to account for energy transport by electron conduction, with  $n_e$  the number of electrons per a.m.u.,  $A$  the average atomic mass,  $Z = An_e$  the average ionic charge, and  $T_7$  the temperature in  $10^7$  K. The radiative (Rosseland) opacity and the conductive opacity are harmonically added. The total opacity is, hence, given by  $\chi = (\bar{\kappa}_{\text{Ross}}^{-1} + \kappa_{\text{con}}^{-1})^{-1}$ .

Once eq. (1) is integrated to  $\tau_{\max}$ , a complete macroscopic description of the atmosphere structure is at hand.

## 2.2. Radiation transfer

For the assumption given above, the radiation transfer equation takes the form

$$\mu \frac{dI_\nu(\mu)}{d\tau_\nu} = I_\nu(\mu) - S_\nu, \quad (3)$$

with  $\mu = \cos \theta$  the cosine of the angle between the normal to the atmosphere and the direction of the considered radiation beam,  $\tau_\nu$  the frequency dependent optical depth,

$I_\nu(\mu)$  the frequency and angle dependent specific intensity, and  $S_\nu$  the source function. With the isotropic and coherent Thomson scattering term, the source function is given by

$$S_\nu = \frac{\kappa_\nu}{\kappa_\nu + \sigma_e} B_\nu + \frac{\sigma_e}{\kappa_\nu + \sigma_e} J_\nu \quad (4)$$

with  $\kappa_\nu$  the frequency dependent OPAL opacity,  $B_\nu$  the Planck function and  $J_\nu$  the mean intensity. We use as boundary conditions for eq. (3)  $I(\mu < 0) = 0$  at  $\tau_{\min}$  and the diffusion approximation at  $\tau_{\max}$ . Equation (3) is solved using the well-documented Rybicki method (e.g. Mihalas 1978).

From the resulting angle dependent specific intensities the flux at the surface of the atmosphere is computed,

$$F_\nu = \int_0^1 \mu I_\nu(\mu) d\mu \Big|_{\tau = \tau_{\min}}. \quad (5)$$

Radiative and conductive equilibrium requires

$$\int_0^\infty F_\nu d\nu + F_{\text{cond}} = \frac{\sigma T_{\text{ns}}^4}{\pi} \quad (6)$$

at each depth in the atmosphere, where  $\sigma$  is the Stefan-Boltzmann constant,  $F_{\text{cond}} = (16\sigma T^3) / (3\rho\kappa_{\text{con}}) dT/dz$  is the conductive energy flux, as detailed in RR96, and  $T_{\text{ns}}$  is the effective temperature of the neutron star. If the deviations from the equilibrium (6) are larger than a given error, correction terms  $\Delta T(\tau)$  are computed from linearization of the angle-integrated form of eq. (3) (e.g. Feautrier 1964; Auer & Mihalas 1969, 1970; Gustafsson 1971).

## 2.3. Model atmosphere computation

The actual computation of a model atmosphere and the emergent spectrum is done in two separate stages.

(i) Starting from the temperature structure of a grey atmosphere (Chandrasekhar 1944), we iteratively construct (Sect. 2.1 and Sect. 2.2) an atmosphere structure that satisfies radiative and hydrostatic equilibrium. At this stage, we use an energy grid of 1000 logarithmic equidistant bins covering the range  $10^{-3.4} - 10$  keV. For each energy bin 30 evaluations of the OPAL opacity tables are harmonically added for the computation of the radiative absorption coefficient. The atmosphere structure is constructed on an optical depth grid with 100 points covering  $\tau_R = 10^{-6} - 5 \times 10^3$  (except for the coldest models, which were computed on a grid covering  $\tau_R = 10^{-6} - 10^3$  due to limitations in the available OPAL data). The angular dependency of the radiation field is sampled by three Gaussian points in  $\mu$ . Radiative equilibrium (eq. 6 is satisfied to better than  $10^{-5}$  at each optical depth) is reached after  $\sim 5 - 15$  iterations. Generally, the hydrogen atmospheres converged the slowest, as the steep drop of the opacity  $\propto \nu^{-3}$  makes the atmosphere transparent for high-energy photons, thus radiatively coupling the deep hot

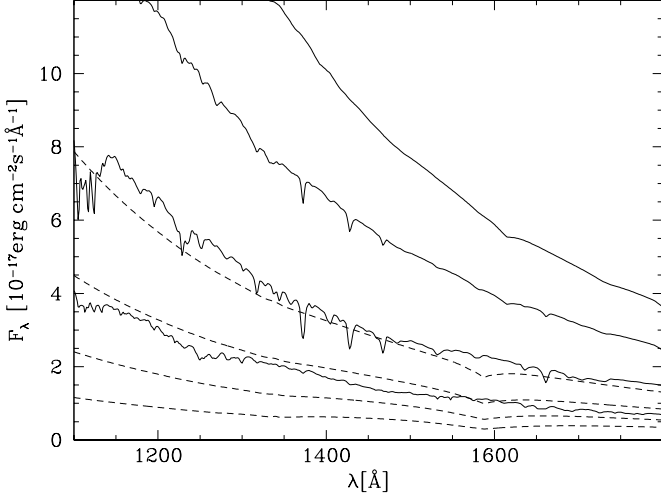


**Fig. 2.** Ultraviolet model spectra of non-magnetic neutron stars in the wavelength range observable with HST/STIS, redshifted for  $z = 0.306$ . Solid lines: iron composition. Dashed lines: hydrogen composition. From top to bottom:  $\log T_{\text{ns}}[K] = 5.7, 5.5, 5.3, 5.1$ . The absolute fluxes are given for  $R_{\text{ns}} = 10 \text{ km}$ ,  $d = 61 \text{ pc}$ , and  $E(B - V) = 0$ , illustrative for the isolated neutron star candidate RX J1856.5-3754 (see Sect. 3).

layers with the surface layers. Electron conduction carries a few percent of the total flux at the largest optical depths (Rosseland optical depths  $\tau_{\text{Ross}} > 100$ ) in the coldest iron and solar atmospheres. For  $\log(T_{\text{ns}}) > 5.75$ , the conductive flux is less than 1%, which is in good agreement with the estimates of ZPS96. Including the conductive opacity in our atmosphere models has, hence, no noticeable effect on the emergent spectra.

(ii) From a given atmosphere structure, we recompute the emergent spectrum solving the radiation transfer (Sect 2.2) on a much finer energy grid (10 000 bins, 10 OPAL evaluations per bin), and using 6 Gaussian points in  $\mu$  to resolve the angular dependence of the specific intensity. The higher number of angular points has practically no influence on the angle-averaged flux from the neutron star surface, but may be used to account for limb darkening in the computation of spectra from neutron stars with non-homogeneous temperature distributions (see Sect. 3).

#### 2.4. The model spectra

We computed grids of model atmospheres for the three different compositions covered by the OPAL opacity/EOS tables: hydrogen, solar abundances, and iron. We restricted ourselves to the canonical neutron star configuration,  $M_{\text{ns}} = 1.4 M_{\odot}$  and  $R_{\text{ns}} = 10 \text{ km}$ , corresponding to a surface gravitational acceleration of  $\log g = 14.386$ . The three grids cover the temperature range  $\log T_{\text{ns}} = 5.1 - 6.5$  in steps of 0.05, i.e. a total of 29 spectra per abundance grid.<sup>1</sup>

<sup>1</sup> The angle-averaged fluxes are available from CDS, for the angle-dependent specific intensities, or models covering addi-

Figure 1 shows the emergent spectra for the three different compositions. As already evident in the previous neutron star atmosphere calculations (R87, RR96, ZVS96), the model spectra differ significantly from blackbody distributions. The pure hydrogen models show a strong flux excess over the blackbody distributions at energies above the peak flux. The free-free and bound-free opacity in these atmospheres drops off rapidly at high energies, leaving Thomson scattering as the dominant interaction between the atmosphere matter and the radiation field. As a consequence, the atmosphere is highly transparent to the hard X-ray photons from deep hot layers. In contrast to the hydrogen models, the iron and solar abundance models are overall closer to the blackbody distributions because of the milder energy dependence of their opacities. They show, however, a substantial amount of absorption structures, lines and edges, which are especially pronounced in the  $\sim 0.1 - 10 \text{ keV}$  range well observable with most of the present and past X-ray satellites.

Noticeable absorption structures with equivalent widths of  $\lesssim \text{\AA}$  are present in the iron spectra of moderately cool neutron stars also in the ultraviolet. The (non-magnetic) hydrogen models contain only the extremely pressure broadened Ly $\alpha$  line. In a magnetic field Ly $\alpha$  splits in three Zeeman-components, with the  $\sigma^+$  component redshifted by  $\sim 100 \text{ \AA}$  for  $B \lesssim 10^9 \text{ G}$ . Because the hydrogen in these hot atmospheres is ionised to a large extent, the Ly $\alpha$  Zeeman components are expected to be rather weak, but they may possibly be detected with future large aperture ultraviolet telescopes, allowing a direct measurement of the magnetic field strength. Figure 2 compares the redshifted<sup>2</sup> iron and hydrogen spectra in the far ultraviolet.

Figure 3 shows the angle-dependent intensity  $I_{\nu}(\mu)$  for a  $T_{\text{ns}} = 10^6 \text{ K}$  iron atmosphere. It is apparent that the emission from the neutron star surface is highly anisotropic, as previously discussed by ZPS96. Calculations of the emission of a neutron star with a non-homogeneous surface temperature distribution must take this anisotropy into consideration. An application of the angle-dependent intensities will be discussed in Sect. 3.

#### 2.5. Comparison to earlier neutron star atmosphere models

##### 2.5.1. Rajagopal & Romani (1996)

The new model spectra agree quite well with the models of RR96. The only systematic differences are found for the hydrogen models, where the new models have a significantly lower flux at energies  $\gtrsim 1 \text{ keV}$  (Fig. 4). This difference is due to the inclusion of Thomson scattering in the new models, which increases the opacities at large optical depths in the hydrogen atmospheres. For the heavy ele-

tional temperatures/surface gravities, please contact the authors.

<sup>2</sup>  $z = (1 - 2GM_{\text{ns}}/R_{\text{ns}}c^2)^{-1/2} - 1 = 0.306$  for an assumed  $R_{\text{ns}} = 10 \text{ km}$  and  $M_{\text{ns}} = 1.4 M_{\odot}$ .

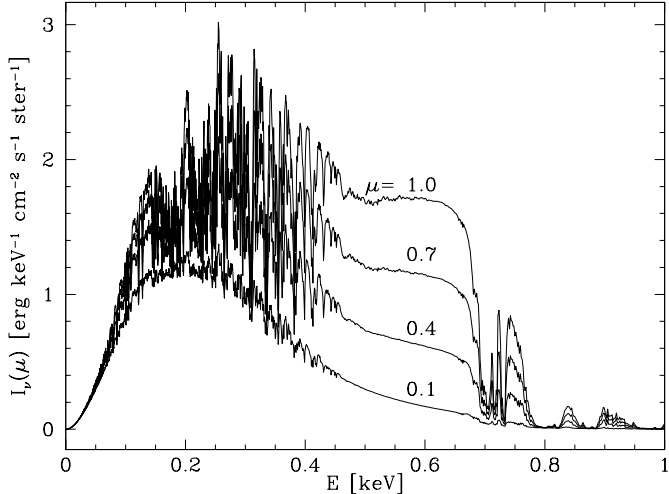


**Fig. 3.** The angle-dependent specific intensity  $I_\nu(\mu)$  of a  $T_{\text{ns}} = 10^6$  K iron model for  $\mu = 1.0, 0.7, 0.4$ , and  $0.1$ .

ment atmospheres, this effect is negligible, as the opacity is dominated by bound-bound and bound-free absorption.

Small (5–15 %) differences in the emergent flux of the heavy element atmospheres are found in the low-temperature ( $\log T_{\text{ns}} \leq 5.75$ ) models in the energy range 1–10 keV. The specific intensities at these high energies are 15–25 orders of magnitude below the peak intensities, and we believe that the differences between the new models and those of RR96 are due to the different numerical treatment of the radiation transfer. At higher energies, the agreement between the two different model generations is better than 1%, except in strong lines where different energy sampling naturally leads to somewhat larger discrepancies.

### 2.5.2. Zavlin et al. (1996)

ZVS96 computed grids of non-magnetic neutron star LTE model atmospheres for three different compositions, hydrogen, helium, and iron. The hydrogen and helium opacities and non-ideal EOS employed in these models were calculated by ZVS96 using the occupation probability formalism described by Hummer & Mihalas (1988). The iron models were computed using the same OPAL data used also by RR96 and in the present paper. Figure 4 compares the ZVS96 iron and hydrogen spectra for  $T_{\text{ns}} = 10^6$  K with models from our new grid and with the RR96 models. The iron models show a significant difference both in the overall shape of the continuum as well as in the details of the absorption features. We traced this to an erroneous use of the opacity grid in ZVS96. This has been confirmed (Pavlov, pri. comm.)<sup>3</sup>. Since the ZPS96 spectral grid has been widely used to fit ROSAT and other neutron star data before 2000, we feel it important to point out these

<sup>3</sup> After we alerted G. Pavlov to their errors in employing the opacities, their group have computed revised models in reasonable agreement with other work. An example revised spectrum appears in (Pavlov & Zavlin 2000).

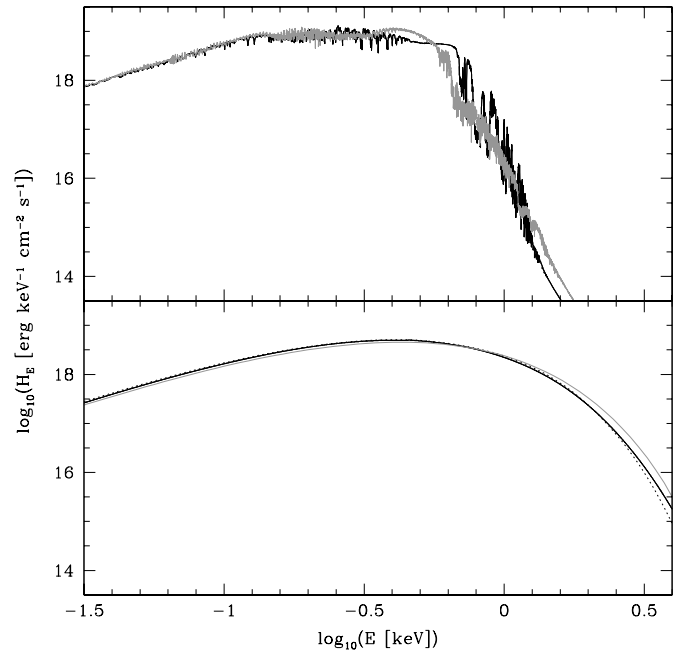


**Fig. 4.** Comparison of  $T_{\text{ns}} = 10^6$  K model spectra for a pure iron (top panel) and hydrogen (bottom panel) atmosphere. The new models are plotted as black solid lines, the RR96 models as black dotted lines, and the ZVS96 models as grey lines (all unredshifted Eddington fluxes). The new iron model and that of RR96 show no visible differences.

errors in the early models that may necessitate revised parameter fits. The ZVS96 hydrogen model is somewhat harder than both our new spectrum and that of RR96. The flux excess of the ZPS96 model (or the flux deficiency of our model) is not fully understood, but likely stems from small differences in the absorption opacity and EOS.

### 2.5.3. Werner & Deetjen (2000)

Werner & Deetjen (2000) presented the first NLTE calculation for a neutron star atmosphere using bound-free opacities from the Opacity Project (Seaton et al. 1994) and explicitly treated line blanketing by millions of lines from the Kurucz & Bell (1995) line list. Figure 5 compares the  $T_{\text{ns}} = 200\,000$  K pure iron NLTE model from Werner & Deetjen (2000) with a corresponding model from our LTE calculations. While the NLTE model clearly shows more detail because of the much larger number of considered transitions, the overall agreement between the two models is very good. Werner & Deetjen (2000) quote a flux difference between their LTE and NLTE models of  $\sim 10\%$  in the line cores, and much less in the continuum. For higher temperatures, the NLTE effects might be stronger, but so far no detailed atomic data are available.

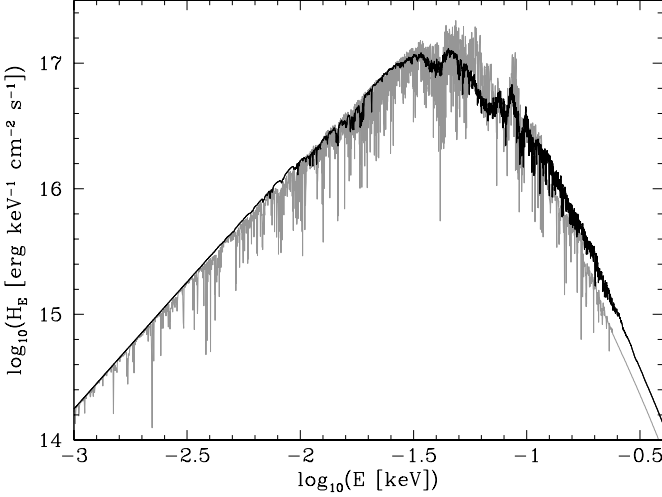


**Fig. 5.** Comparison of the  $T_{\text{ns}} = 200\,000\text{ K}$  pure iron NLTE model spectrum from Werner & Deetjen (2000) (gray curve, unredshifted Eddington flux) with a corresponding LTE model spectrum from our new atmosphere grid (curve).

### 3. An application: The bright isolated neutron star RX J1856.5–3754

RX J1856.5–3754 is the X-ray brightest isolated neutron star<sup>4</sup> (INS) candidate (Walter et al. 1996, see Treves et al. (2000) for a review of INS). Although the exact nature of these neutron stars is still controversial – old neutron stars reheated by accretion (e.g. Treves & Colpi 1991, however, see also Neuhäuser & Trümper 1999) versus young magnetars (e.g. Heyl & Hernquist 1998b) – it is generally believed that the emission of these objects is dominated by thermal emission from the neutron star surface.

The ROSAT PSPC data of RX J1856.5–3754 were previously analyzed by Pavlov et al. (1996), using the model spectra from ZVS96. They found that the data are best described either by a pure iron model or by a blackbody spectrum. Non-magnetic hydrogen and helium atmospheres could be excluded as they imply a distance of only a few pc, and as they overpredict the  $V$  magnitude by large factors. The distances derived from the model normalizations,  $216 \pm 33\text{ pc}$  and  $158 \pm 26\text{ pc}$  for the iron model and the blackbody spectrum, respectively, greatly exceed, however, the recently measured distance of RX J1856.5–3754,  $d = 61 \pm 9\text{ pc}$  (Walter 2001). Pavlov et al. (1996) also fitted a magnetic hydrogen model ( $B = 10^{12}\text{ G}$ ) to the ROSAT data, which provided the worst fit and implied a distance of  $12.1 \pm 1.3\text{ pc}$ .

As a first application of our new model spectra, we present a re-analysis of the archival ROSAT PSPC observations of RX J1856.5–3754. We have extracted source and background spectra from the single existing (off-

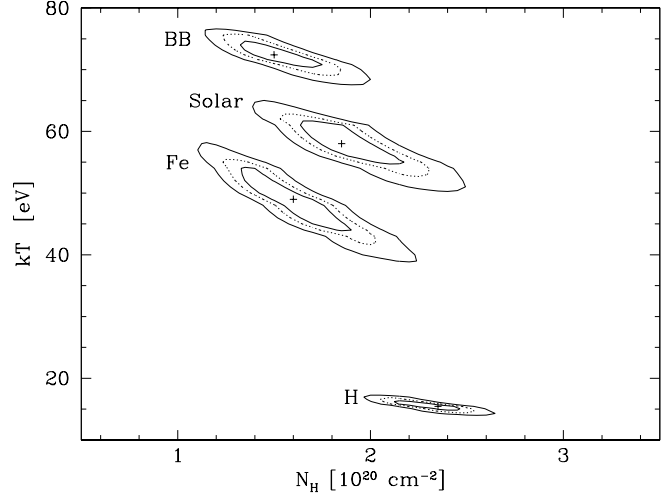


**Fig. 6.** Confidence contours of the spectral fits (Table 1) to the RX J1856.5–3754 ROSAT PSPC data. Shown are the 68.1%, 90%, and 99% confidence levels.

**Table 1.** Best-fit parameters from the analysis of the ROSAT PSPC data of RX J1856.6–3754. Listed are the effective temperature at the neutron star surface, the interstellar column density of neutral hydrogen, the distance derived from the model normalization (assuming  $R_{\text{ns}} = 10\text{ km}$ ), the reduced  $\chi^2$ , and the visual magnitude of the redshifted surface emission. The *observed* neutron star temperature and radius are defined by  $T_{\infty} = T_{\text{ns}}(1+z)^{-1}$  and  $R_{\infty} = R_{\text{ns}}(1+z)$ .

	$kT_{\text{ns}}$ [eV]	$N_{\text{H}}$ [ $10^{20}\text{ cm}^{-2}$ ]	$d$ [pc]	$\chi^2_{\text{red}}$	$V$
BB	$72.3 \pm 1.2$	$1.51 \pm 0.15$	$151 \pm 20$	1.62	26.1
Fe	$49.0 \pm 1.9$	$1.59 \pm 0.19$	$54 \pm 10$	1.73	24.6
Solar	$58.1 \pm 2.9$	$1.87 \pm 0.20$	$84 \pm 14$	1.82	25.4
H	$15.6 \pm 3.5$	$2.29 \pm 0.18$	$3.4 \pm 0.4$	1.73	20.1

axis) ROSAT PSPC observation of RX J1856.5–3754 using the EXSAS (Zimmermann et al. 1994) package. We find a vignetting-corrected count rate of  $3.65 \pm 0.03\text{ cts s}^{-1}$ , which agrees very well with the result of Walter et al. (1996). Source and background spectra as well as the response matrices were exported in an XSPEC-compatible format. Using XSPEC 11.0.1, we then fitted the X-ray spectrum of RX J1856.5–3754 with our model spectra (converted to XSPEC additive table models) and with a simple blackbody spectrum. The absorption column was a free parameter and we fixed the redshift to  $z = (1 - 2GM_{\text{ns}}/R_{\text{ns}}c^2)^{-1/2} - 1 = 0.306$ , corresponding to a canonical neutron star configuration,  $M_{\text{ns}} = 1.4 M_{\odot}$ ,  $R_{\text{ns}} = 10\text{ km}$ . The best-fit parameters are reported in Table 1; the corresponding confidence regions in the  $N_{\text{H}} - T_{\text{ns}}$  plane are shown in Fig. 6.

As expected, the results of the blackbody fit agree well with the parameters derived by Pavlov et al. (1996). The best-fit temperature of our iron atmosphere is somewhat

<sup>4</sup> The term “isolated neutron stars” might be misleading: the bulk of known neutron stars are active radio pulsars, and most of them are single stars. A more appropriate name would be “radio-quiet neutron stars.”

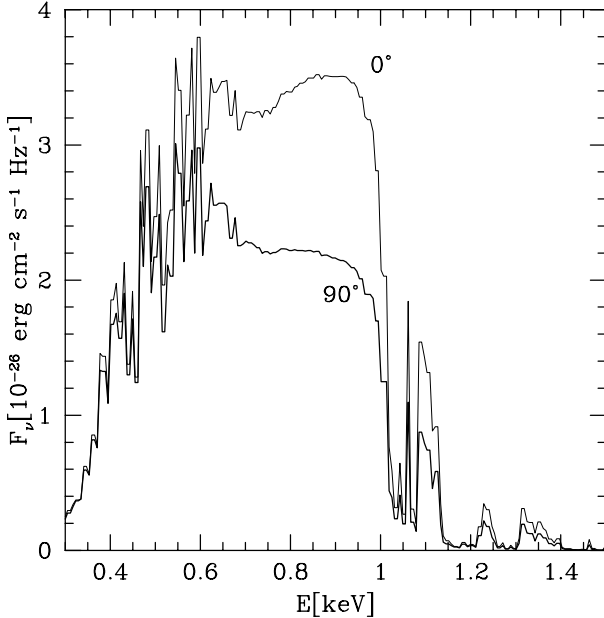


**Fig. 7.** Example spectra for  $\alpha = 60^\circ$ ,  $\zeta = 70^\circ$ . Dark curve: spectrum from middle of main pulse. Light curve: spectrum from off pulse. Note the increase in continuum at 0.5–1.0 keV and the variations in line strengths, both direct effects of limb darkening.

lower than that of Pavlov et al. (1996), and, the distance that we derive from our fit is consistent with the measured parallax. We attribute these different results to the wrong emergent spectra used by Pavlov et al. (1996, see Sect. 2.5.2)

Our solar abundance atmospheres provide a similarly satisfying fit. Just as in Pavlov et al. (1996), we can exclude a non-magnetic hydrogen atmosphere, as the implied distance and the predicted visual magnitude are totally inconsistent with the observations.

Both the iron and the solar best-fit models slightly *overpredict* the visual flux. This finding is in agreement with a recent analysis of a detailed multi-wavelength study of RX J1856.5–3754 (Pons et al. 2001). Pons et al. (2001) argue that a satisfying fit to the overall spectral energy distribution can be achieved by assuming an inhomogeneous surface temperature distribution. While a full analysis of the available multi-wavelength data is beyond the scope of the present simple application, we use here our angle-dependent intensities to discuss the implications of a two-zone polar cap model on the observed X-ray light curve of RX J1856.5–3754.

Using the Monte Carlo code described in Braje et al. (2000), we modeled the thermal emission. This code includes a complete treatment of the surface beaming, as well as full General Relativistic computations of the photon paths. Doppler boosting and Kerr effects are included in the code, but we assume here that RX J1856.5–3754 is a slow rotator so that these are negligible. Following the best-fit parameters of Pons et al. (2001), we chose a

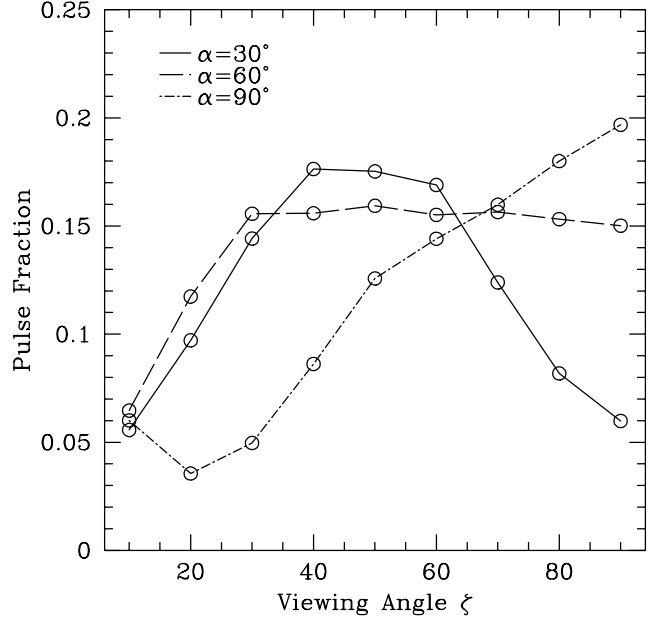


**Fig. 8.** Pulse fraction as a function of  $\zeta$ . The three curves represent three different values of  $\alpha$ . Note that the curves peak near the expected values:  $\alpha = \zeta$ .

two temperature, two polar cap model with a polar cap half-angle size of  $24^\circ$ . We set the cap temperature to be  $9.3 \times 10^5$  K and the uniform surface component to be  $1.7 \times 10^5$  K. We adopt  $R_{\text{ns}} = 10$  km, but following Pons et al. (2001), use  $M_{\text{ns}} = 1.8M_\odot$ . The effect of the increased gravity on the emergent spectral lines and edges is small (R87); we can thus use our standard grid atmospheres while accounting for the increased redshift and gravitational focusing. We employ a fiducial 1s rotational period and compute models for  $\alpha$  (angle between rotational and polar cap axes) of  $30^\circ$ ,  $60^\circ$ , and  $90^\circ$ . We adopt a hydrogen column density  $N_{\text{H}} = 1.4 \times 10^{20}$  cm $^2$  and a distance of 61 pc.

Upon examination of the results, we find that, even with the strong General Relativistic smearing of a  $1.8M_\odot$  star, for almost any viewing angle  $\zeta$ , it is very difficult to produce a pulse fraction as low as 6%, the upper limit on the variability of RX J1856.5–3754 derived from the ROSAT data (Pons et al. 2001). In fact, pulse fractions below 10% are only seen for  $\zeta$  smaller than  $20^\circ$  (for any  $\alpha$ ) or for  $\alpha \lesssim 30^\circ$  and  $\zeta \gtrsim 80^\circ$  (Fig. 8). These large pulse fractions are a direct result of limb darkening effectively beaming the radiation from the surface. Furthermore, limb darkening has a substantial effect on the shape of the spectrum emerging from different parts of the pulse (see Figure 7). There is a strong over-all shape (temperature) shift as well as variations in the line strengths. Energy-dependent limits on the pulse fraction can thus place even stronger constraints on models with non-uniform surface temperatures.

#### 4. Beyond “classic” stellar atmospheres

As in previous calculations (R87, RR96, ZVS96, Werner & Deetjen 2000), the model atmospheres presented here assume radiative equilibrium. It is worth remembering that when model fits suggest that the flux is dominated by hot polar caps with a small fraction of the full neutron star surface area, some sort of local heating is likely implicated. For instance, anisotropic interior conductivities can produce smooth variations in the surface effective temperature; e.g. Heyl & Hernquist (1998a). For slow, long  $P$  neutron stars, local heating can be caused by low  $\dot{M}$  accretion. Zampieri et al. (1995) and Zane et al. (2000) have produced emergent spectra for ionized H stars accreting at low rates. With proton stopping depths of  $\sim 20 \text{ g cm}^{-2}$ , much of the energy is deposited fairly deep in the atmosphere, but shocks in the accretion flow can apparently heat the outer layers, providing excess flux on the Rayleigh-Jeans tail. For an active magnetosphere, local heating without accretion arises from precipitating  $e^\pm$  (Arons 1981) or from illumination by energetic (polar cap or outer gap) photons. Electron/positron energy is largely deposited in the surface layers  $\sim 0.1 \text{ g cm}^{-2}$ , while photon absorption depths depend strongly on the spectrum and ionization state of the atmosphere.

An analogue situation – pole caps heated by accretion – is well-documented in polars, a subtype of cataclysmic variables in which a strongly magnetic white dwarf accretes from a late type donor star. In these systems, the white dwarf atmosphere near the magnetic poles is heated by strong irradiation with cyclotron radiation and thermal bremsstrahlung from a stand-off shock. As a consequence of this accretion heating, the spectra of these heated pole caps are almost devoid of spectral structures. The Lyman lines, typically very strong absorption features in the ultraviolet spectra of white dwarfs, are almost completely flattened out (Gänsicke et al. 1998), and also the X-ray spectrum is very close to blackbody emission, much unlike the expected emission from a high-gravity photosphere strongly enriched with heavy elements (Mauche 1999). While the physical processes involved in heating the pole caps of accreting white dwarfs and accreting neutron stars differ markedly, the observed phenomenology is very similar: RX J0720.4-3125, another bright isolated neutron star shows a quasi-sinusoidal X-ray light curve suggesting the presence of large heated pole caps, whereas the X-ray spectrum contains no significant absorption structure (Haberl et al. 1997; Paerels et al. 2001) reminiscent to the ultraviolet observations of the heated white dwarf in the polar AM Her (Gänsicke et al. 1998). It appears, therefore, likely that heating effects may affect the line spectra of heavy element neutron star atmospheres.

As a simple illustration, we ignored the details of particular physical heating effects and computed a number of spectra under the assumption that an energy  $\alpha\sigma T_{\text{ns}}^4$  is deposited at a characteristic depth in the atmosphere,  $\tau_{\text{dep}}$  (Fig. 9). In practice, the emergent spectrum of a “heated” neutron star is computed by (1) modifying the ther-

mal structure of an undisturbed atmosphere  $T(\tau)$  to account for the deposited energy, (2) recomputing the atmosphere structure based on the modified temperature profile (Sect. 2.1), and finally solving the radiation transfer within the “heated” atmosphere (Sect. 2.2). Figure 10 shows the emergent fluxes from a  $T_{\text{ns}} = 10^6 \text{ K}$  iron atmosphere for two different sets of parameters,  $\alpha = 0.82$  and  $\tau_{\text{dep}} = 1$ , equivalent to  $\Sigma = 3.2 \times 10^{-3} \text{ g cm}^{-2}$ , and  $\alpha = 0.035$  and  $\tau_{\text{dep}} = 0.01$ , equivalent to  $\Sigma = 2.2 \times 10^{-4} \text{ g cm}^{-2}$ .

Two effects are evident. The flatter temperature in the outer layers of the heated atmospheres suppresses the strong absorption edge around 1 keV, returning the Wien tail colour quite close to that of a simple blackbody. Further, the equivalent widths of the lines are, of course, strongly affected. Heating at  $\tau \sim 1$  strongly suppresses the  $\leq \text{keV}$  absorption features; surface heating in fact drives the line features on the Rayleigh-Jeans tail into emission.

We stress that this illustrative approach is by no means a self-consistent model of a heated neutron star atmosphere, as we do not include neither any physical assumption on the actual heating mechanisms, nor a proper energy balance of the heating/cooling processes. It is merely intended as a possible explanation for the apparent paradox that the observations of isolated neutron stars (in particular RX J1856.5-3754) are best-fitted with heavy-element model spectra (Pavlov et al. 1996; this paper; Burwitz et al. 2001; Pons et al. 2001), whereas their X-ray spectra show at best very weak spectral structures.

More detailed future work will need to carefully examine the efficiency of the various possible heating mechanisms, in particular to establish the depth-dependent energy deposition, and to account properly for the energy balance in the neutron star atmosphere.

#### 5. Conclusions

We have presented a set of angle-dependant low field neutron star atmosphere spectra. These radiative and hydrostatic equilibrium atmospheres should be useful to researchers pursuing exploratory fits of soft X-ray/UV/optical data. However, it is important to inject a note of caution into the discussion. At a minimum, non-uniform surface temperature, combined with limb-darkening and gravitational focussing will have subtle, but important effects (which can be modeled using the present grid (Sect. 3)).

Many other physical effects can, of course, strongly perturb neutron star spectra. The effects on heavy element absorption lines and edges can be particularly strong. Magnetic fields characteristic of young radio pulsars will have a dramatic effect on the opacities and the emergent spectra. When considering the strength of the absorption lines in spectra from magnetic atmospheres with heavy elements (Rajagopal et al. 1997) it is important to remember that the line energies depend sensitively on the B-field. Even simple dipole  $B$  variation across a polar cap can shift line energies by  $\sim 10\%$ , strongly decreasing the equivalent width of spectral features in phase-averaged spectra.

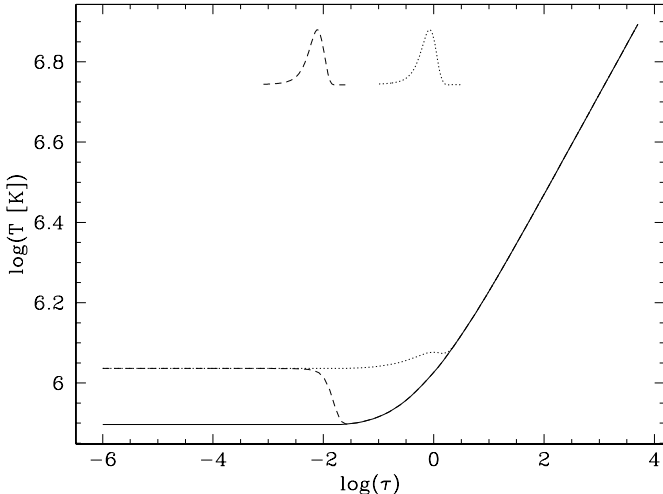


**Fig. 9.** Temperature structures  $T(\tau)$  in a locally heated  $^4$  neutron star atmosphere. An energy amount of  $0.035\sigma T_{\text{ns}}^4$  ( $0.82\sigma T_{\text{ns}}^4$ ) is deposited at an optical depth  $\tau_{\text{dep}} = 0.01$  ( $\tau_{\text{dep}} = 1$ ). This energy injection is spread by a Gaussian distribution with a width of  $\log \tau = 0.3$ , as illustrated in the figure, avoiding unrealistic (and numerically problematic) step functions in the  $T(\tau)$  structure. The undisturbed temperature run is plotted as solid line, the atmosphere heated at  $\tau = 0.01$  ( $\tau = 1$ ) as dashed (dot-dashed) line.

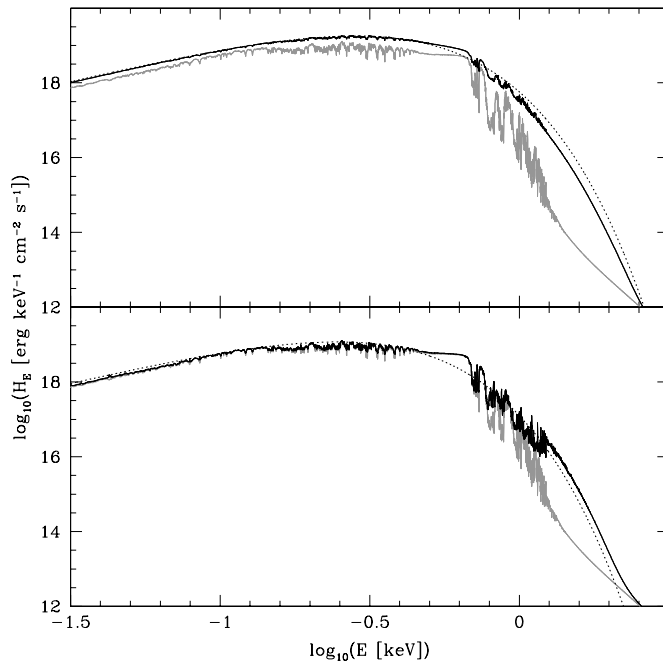


**Fig. 10.** Emergent spectra from a heated  $T_{\text{ns}} = 10^6$  K iron atmosphere. Top panel:  $0.82\sigma T_{\text{ns}}^4$  are deposited at  $\tau_{\text{dep}} = 1$ , equivalent  $\Sigma = 3.2 \times 10^{-3} \text{ g cm}^{-2}$ . The spectrum of the heated atmosphere and of the undisturbed atmosphere are plotted as black and as gray lines, respectively. The dashed line shows a blackbody spectrum corresponding to the effective temperature of the heated atmosphere. Bottom panel:  $0.035\sigma T_{\text{ns}}^4$  are deposited at deposited at  $\tau_{\text{dep}} = 0.01$ , equivalent  $\Sigma = 2.2 \times 10^{-4} \text{ g cm}^{-2}$ .

Convection has also been considered (eg. RR96), although even small magnetic fields may suppress convective transport and keep atmospheres close to the hydrostatic solution.

In sum, while we feel that our atmosphere grid should be of use for fitting of observed data, complications to the models are certainly expected. In particular strong  $B$ -field variations and surface re-heating can decrease the equivalent width of heavy element line features in neutron stars with active magnetospheres; this may explain in part the difficulty in finding such features in early *CXO/XMM* data (e.g. Paerels et al. 2001).

*Acknowledgements.* BTG was supported in part by a travel grant of the Deutscher Akademischer Auslandsdienst (DAAD) and by the DLR under grant 50OR99036. We thank K. Werner and G. Pavlov for providing their model spectra for a quantitative comparison, and B. Rutledge for comments on an earlier draft. The referee, Dr. Zavlin, provided a number of helpful comments.

## References

Arons, J. 1981, *ApJ*, 248, 1099  
 Auer, L. H. & Mihalas, D. 1969, *ApJ*, 158, 641  
 —. 1970, *MNRAS*, 149, 65  
 Braje, T. M., Romani, R. W., & Rauch, K. P. 2000, *ApJ*, 531, 447  
 Burwitz, V., Dennerl, K., Haberl, F., Neuhäuser, R., Predehl, P., Zavlin, V. E., Reinsch, K., & Gänsicke, B. T. 2001, in *X-ray Astronomy 2000*, ed. R. Giacconi, L. Stella, & S. Serio (ASP Conf. Ser. *in press*)  
 Chandrasekhar, S. 1944, *ApJ*, 100, 76  
 Cox, J. P. & Giuli, R. T., eds. 1968, *Stellar Structure*, Vol. I (New York: Gordon & Breach)  
 Feautrier, P. 1964, *C.R. Acad. Sc. Paris*, 258, 3189  
 Gänsicke, B. T., Beuermann, K., & de Martino, D. 1995, *A&A*, 303, 127  
 Gänsicke, B. T., Hoard, D. W., Beuermann, K., Sion, E. M., & Szkody, P. 1998, *A&A*, 338, 933  
 Gustafsson, B. 1971, *A&A*, 10, 187  
 Haberl, F., Motch, C., Buckley, D., Zickgraf, F.-J., & Pietsch, W. 1997, *A&A*, 326, 662  
 Heyl, J. S. & Hernquist, L. 1998a, *MNRAS*, 300, 599  
 —. 1998b, *MNRAS*, 297, L69  
 Hummer, D. G. & Mihalas, D. 1988, *ApJ*, 331, 794  
 Iglesias, C. A. & Rogers, F. J. 1996, *ApJ*, 464, 943  
 Kurucz, R. & Bell, B. 1995, *Atomic Line Data* (R.L. Kurucz and B. Bell) Kurucz CD-ROM No. 23. Cambridge, Mass.: Smithsonian Astrophysical Observatory, 1995., 23  
 Lai, D. 2001, *Rev. Mod. Phys.*, 73, 629  
 Mauche, C. W. 1999, in *Annapolis Workshop on Magnetic Cataclysmic Variables*, ed. C. Hellier & K. Mukai (ASP Conf. Ser. 157), 157—168  
 Mihalas, D. 1978, *Stellar atmospheres*, 2nd edn. (San Francisco: W. H. Freeman & Co)  
 Neuhäuser, R. & Trümper, J. E. 1999, *A&A*, 343, 151  
 Paerels, F., Mori, K., Motch, C., Haberl, F., Zavlin, V. E., Zane, S., Ramsay, G., Cropper, M., & Brinkman, B. 2001, *A&A*, 365, L298

Pavlov, G. G., Shibanov, Y. A., Zavlin, V. E., & Meyer, R. D. 1995, in *The Lives of the Neutron Stars.*, ed. M. A. Alpar, U. Kiziloglu, & J. van Paradijs (Dordrecht: Kluwer), 71–90

Pavlov, G. G. & Zavlin, V. E. 2000, in *Highly Energetic Physical Processes and Mechanisms for Emission from Astrophysical Plasmas*, ed. P. C. H. Martens, S. Tsuruta, & P. Weber (ASP Conf. Ser. 195), 103

Pavlov, G. G., Zavlin, V. E., Truemper, J., & Neuhaeuser, R. 1996, *ApJ Lett.*, 472, L33

Pons, H. A., Walter, F. M., Lattimer, J. M., Prakash, M., Neuhaeuser, R., & An, P. 2001, *ApJ in press* (astro-ph/0107404)

Rajagopal, M. & Romani, R. W. 1996, *ApJ*, 461, 327

Rajagopal, M., Romani, R. W., & Miller, M. C. 1997, *ApJ*, 479, 347

Romani, R. W. 1987, *ApJ*, 313, 718

Rutledge, R. E., Bildsten, L., Brown, E. F., Pavlov, G. G., & Zavlin, V. E. 1999, *ApJ*, 514, 945

—. 2000, *ApJ*, 529, 985

—. 2001, *ApJ*, 551, 921

Seaton, M. J., Yan, Y., Mihalas, D., & Pradhan, A. K. 1994, *MNRAS*, 266, 805

Treves, A. & Colpi, M. 1991, *A&A*, 241, 107

Treves, A., Turolla, R., Zane, S., & Colpi, M. 2000, *PASP*, 112, 297

Walter, F. M. 2001, *ApJ*, 549, 433

Walter, F. M., Wolk, S. J., & Neuhaeuser, R. 1996, *Nat*, 379, 233

Werner, K. & Deetjen, J. 2000, in *Pulsar Astronomy - 2000 and Beyond*, ed. M. Kramer, N. Wex, & R. Wielebinski (ASP Conf. Ser. 202), 623–624

Zampieri, L., Turolla, R., Zane, S., & Treves, A. 1995, *ApJ*, 439, 849

Zane, S., Turolla, R., & Treves, A. 2000, *ApJ*, 537, 387

Zavlin, V. E., Pavlov, G., & Shibanov, Y. 1996, *A&A*, 315, 141

Zavlin, V. E. & Pavlov, G. G. 1998, *A&A*, 329, 583

Zimmermann, H., Becker, W., Belloni, T., Döbereiner, S., Izzo, C., Kahabka, P., & Schwentker, O., eds. 1994, *EXSAS User's Guide*, MPE report 257 (Garching: MPE)